Journal Pre-proofs

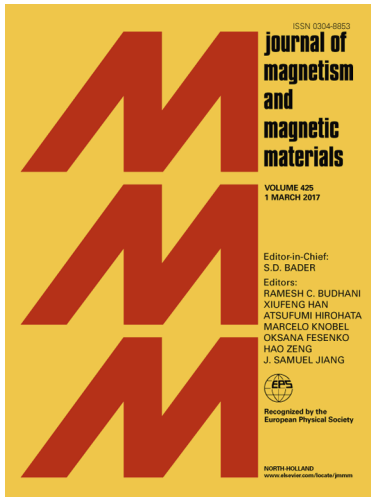

Structural, Electric and Dielectric properties of $Ni_{0.5}Zn_{0.5}FeCoO_4$ ferrite prepared by sol-gel

A. Omri, E. Dhahri, B.F.O. Costa, M.A. Valente

PII: S0304-8853(19)31091-1
DOI: https://doi.org/10.1016/j.jmmm.2019.166243
Reference: MAGMA 166243

To appear in: *Journal of Magnetism and Magnetic Materials*

Received Date: 24 March 2019
Revised Date: 23 September 2019
Accepted Date: 29 November 2019

Please cite this article as: A. Omri, E. Dhahri, B.F.O. Costa, M.A. Valente, Structural, Electric and Dielectric properties of $Ni_{0.5}Zn_{0.5}FeCoO_4$ ferrite prepared by sol-gel, *Journal of Magnetism and Magnetic Materials* (2019), doi: https://doi.org/10.1016/j.jmmm.2019.166243

Structural, Electric and Dielectric properties of $Ni_{0.5}Zn_{0.5}FeCoO_4$ ferrite prepared by sol-gel

A. Omri [1, *], E. Dhahri [1, 2], B.F.O. Costa [3], M.A. Valente [4]

[1] Research Unit of Optimization and Valuation of Resource, Faculty of Science and Technology of Sidi Bouzid University Campus Agricultural City, Sidi Bouzid 9100, University of Kairouan, Tunisia
[2] Laboratory of Applied Physics, Faculté des Sciences de Sfax, Université de Sfax, B.P. 1171, Sfax 3000, Tunisie
[3] CFisUC, Physics Department, University of Coimbra, Rua Larga, 3004-516, Coimbra, Portugal
[4] I3N and Physics Department, University of Aveiro, 3810-193 Aveiro, Portugal

ABSTRACT

$Ni_{0.5}Zn_{0.5}FeCoO_4$ spinel ferrite was elaborated using sol-gel technique. X-ray diffraction patterns indicate that sample has a cubic spinel type structure with Fd-3m space group. The change in Raman modes and relative intensity were observed due to ball milling and consequently to the decrease of particle size and cationic redistribution. The Raman spectra show peaks appearing at 450 and 490 cm^{-1} corresponding to T_2g (2) and T_2g (3), respectively. It may be noted that both of these modes shift toward the higher wavenumber with the substitution of Zn by Ni in $Ni_{0.5}Zn_{0.5}FeCoO_4$ ferrite. Mössbauer spectroscopy analysis shows one tetrahedral A-site and two octahedral B-sites. Due to Zn doping, the hyperfine magnetic fields are much smaller than for $CoFe_2O_4$ and $NiFe_2O_4$ ferrites. The Jonscher's power low was used to describe the ac-conductivity measurements. Frequency dependence of dielectric constant (ε'') and tangent loss ($tan\delta$) display a dispersive behavior at low frequencies that can be explained by the Maxwell Wagner model and Koop's theory. Electric modulus formalism has used to study the relaxation dynamics of charge carriers. The complex impedance spectra (Nyquist plots) show well-defined semicircles which are strongly dependent on the temperature.

Keywords: Ferrites; Mössbauer spectrometry; Dielectric properties; Transport mechanisms.

Corresponding author: ***Aref OMRI omriaref@yahoo.fr***
Tel: +21622220720; Fax: +21674676609.

I. Introduction

With the remarkable progress that the world is witnessing now in all fields, the synthesis and characterization of nanomagnetic materials have attracted much of scientists' attention because of their widespread fundamental and technological importance depending upon their unique physical and chemical properties. Among nanomagnetic materials, spinel ferrites MFe_2O_4 (M = Fe, Mn, Zn, Mg, Co...) show important structural, morphological, chemical, magnetic, mechanical thermal, optical and electric properties [1-4]. These materials have a variety of promising technological applications such as high-density recording devices, color imaging, ferrofluids, magnetic refrigerators, and high-frequency devices [5-9]. In addition, their high values of electrical resistivity and their low eddy current losses make them ideal for the use in microwave devices [10, 11]. On the other hand, spinel ferrites present excellent biocompatibility, chemical stability under physiological conditions [12, 13].

The spinel structure of the soft magnetic ferrites has the chemical formula of $(A)[B]_2O_4$, where A expresses the cations distribution in the tetrahedral sites and B represents the octahedral cations position. However, in the case of spinel ferrites, the chemical formula $(A)[Fe]_2O_4$ represents many possible intermediary cation distributions that denote considerable cation disorder, indicating that spinel ferrites structure requires special attention regarding magnetic characterization [14]. The spinel crystal structures are usually categorized by inverse and normal structures. In the normal spinel or "direct" structure, A is a divalent element atom, occupying tetrahedral A sites, while B is a trivalent element sitting on the octahedral B sites. When A is a trivalent element which occupies the tetrahedral site and B consists of equal numbers of trivalent and divalent elements, distributed over octahedral sites, the spinel structure is referred to as the inverse kind [15-18].

In order to study the electrical properties of ferrite materials, the complex impedance spectroscopy (CIS) was used. The CIS technique is appropriate for the transport process under study. The commonly used models for the CIS are electrical equivalent circuits consisting of resistors, capacitors, inductors and specialized distributed elements. The necessary information about the dielectric properties of materials can be also obtained from the complex impedance analysis. The impedance analysis allows separation of several contributions of total impedance, arising from the bulk conductance and interfacial phenomenon viz. grain, grain boundary and other electrode interface effects.

In the present work, we have prepared a ferrite sample with $Ni_{0.5}Zn_{0.5}FeCoO_4$ composition by sol-gel technique and we present its structural, morphology, Raman and Mössbauer properties. Then, the dielectric and impedance spectroscopy results are discussed in the frequency range of 100 Hz to 1 MHz by varying temperature from 150 K to 200 K.

II. Experimental

$Ni_{0.5}Zn_{0.5}FeCoO_4$ ferrite was synthesized via sol-gel method[19] using $Ni(NO_3)_2.6H_2O$, $Co(NO_3)_2.3H_2O$, $Zn(NO_3)_2.6H_2O$ and $Fe(NO_3)_3.9H_2O$ nitrates. The stoichiometric amounts of these nitrates were firstly dissolved in distilled water under regular stirring at 373 K on hot plate. Controlled quantities of citric acid which is used as complexation agent and ethylene glycol used as polymerization agent were added to the mixed solution. The pH of the solution was adjusted to about 7 by the addition of ammonia. Heating with stirring is continued until the formation of gel after approximately 4 h. The gel was dried at 573 K for 12 h. The resulting powder has undergone several grindings, pelleting and sintering cycles, and the desired crystalline phase for $Ni_{0.5}Zn_{0.5}FeCoO_4$ compound was well formed at 1373 K.

X-ray diffractometer (Bruker 8D Advance X-ray powder) using Ni-filtered CuK_α radiation (λ=15.41 nm) was used to record the X-ray diffraction (XRD) pattern in 20°-100° angular range. Scanning electron micrographs (SEM) were taken with *TESCAN VEGA3 SBH* microscope equipped with an EDS detector Burker XFlagh 410M. So that energy dispersive X-ray analysis (EDXA) was also done. A PerkinElmer STA6000 system was used to perform the Differential Scanning Calorimetry (DSC) with a step of 20 °C min^{-1}. Raman spectra for $Ni_{0.5}Zn_{0.5}FeCOO_4$ sample were obtained in the wave number range 50–1500 cm^{-1} using a Raman micro-system (Horiba LabRam HR Evolution) equipped with a high-stability BXFM open space confocal microscope, a Synapse CCD detector, and a 600 g mm^{-1} grating, with 532 nm excitation. The room temperature Mössbauer spectra were recorded in transmission geometry, in a WissEL spectrometer, using the ^{57}Fe as isotope and a source of ^{57}Co (energy of 14.4 keV) in a matrix of Rh with an activity of about 20 mCi. The spectra were fitted by a set of Lorentzian lines determined by the least squares method using the NORMOS program distributed by WissEL GmbH. Isomer shifts is given relative to α–Fe. Two parallel plate electrodes have been used to achieve the dielectric measurements of the pellet in between them.

The dielectric measurements were performed in a temperature range between 140 and 370 K, using a nitrogen bath cryostat setup. During the measurements, the samples were kept in a helium

atmosphere to minimize thermal gradients and the temperature of the samples was controlled by an Oxford Research IT-C4 and measured using a platinum sensor. The impedance of the samples was measured with an Agilent 4294 Network Analyzer, operating between 100 Hz and 1 MHz in the Cp-Rp configuration (capacitance in parallel with resistance) [43].

III. Results and discussion

3.1 Structural analysis

XRD pattern for $Ni_{0.5}Zn_{0.5}FeCoO_4$ sample recorded at room temperature is shown in **Fig.1**. This figure shows the reflections allowed in the cubic spinel structure as the diffraction planes (220), (311), (222), (400), (422), (511), (440), (620), (533), (444), (731), and (800). Also, the XRD pattern confirmed the formation of single phase of the sintered $Ni_{0.5}Zn_{0.5}FeCoO_4$ ferrite sample. The lattice parameters, a, and volume, V, were calculated from the XRD pattern and are 8.418(1) Å and 596.63(2) $Å^3$, respectively.

. Average grain size (d_{sc}) were calculated from XRD peaks using the Scherer formula[25]:

$$d_{sc} = \frac{0.9\,\lambda}{\beta \cos\theta_{311}} \qquad (3)$$

where λ is the X-ray wavelength used in the measurement, θ_{311} is the diffraction angle for the most intense peak (311) and β is the half height width of this peak. The average grain size was estimated as 2.2±0.01 μm.

Fig. 2a represents the SEM image of the free surface of $Ni_{0.5}Zn_{0.5}FeCoO_4$ compound. The difference in microstructure is clearly seen concerning the grain size and morphology. It consists of both large and small agglomerated grains at the surface of the higher nickel containing sample and characterized by various shapes with some micro-pores, which is in line with our previous results[20-25]. The presence of the microstructural characteristics can be related to the matter transport mechanism between the near grains during the sintering process. **Fig. 2b** shows the size distribution of the sample determined using *image J* software. As observed, the histogram is well modelated by a Gaussian function. The estimated average grain size is about 330±0.2 nm, which is higher than the crystallite size previously determined from the Scherer formula. This is due to the fact that each particle observed by SEM consists of several crystallite domains. The average agglomeration rate, defined as the ratio of the average grain size on that of crystallite, was found to be 16.4±0.1 μm. **Fig. 3** shows the energy dispersive X-ray analysis (EDAX) spectrum at room temperature for $Ni_{0.5}Zn_{0.5}FeCoO_4$ compound. This analysis showed that the chemical

composition of the compound was close to that of the nominal one (Ni: Fe: Co: Zn = 0.5: 1: 1: 0.5), within experimental uncertainties.

3.2. Raman and calorimetry measurements

Raman Spectroscopy is one of the vital characterization techniques used to investigate the vibration motion of the molecules and to verify the presence of different structural phases. In the spinel ferrites group, theory predicts five active Raman modes ($A_{1g}+E_g+3T_{2g}$) related to vibrations of metal cations and oxygen O^{2-} with different frequencies depending on octahedral or tetrahedral coordination, with three of them frequently observed. Besides, cation ordering promotes the activation of additional vibration modes[26, 27]. The A_{1g} is the symmetric stretch of tetrahedral FeO_4 and appears around 600-720 cm^{-1}. The E_g is due to symmetric bending of oxygen ions for Fe and peaks around 250-360 cm^{-1}. The three T_{2g} modes appear due to anti-symmetric bending/stretching of ligands. The T_{2g} (3) is an anti-symmetric bending of oxygen concerning Fe and appears around 500-590 cm^{-1}, T_{2g} (2) is an anti-symmetric stretch of Fe and O and gives rise to a peak around 450-520 cm^{-1} and T_{2g} (1) is the translational motion of Fe-O reflected close to 180 - 220 cm^{-1}[26,27].

Room temperature Raman spectra were recorded for $Ni_{0.5}Zn_{0.5}FeCoO_4$ sample in the energy range of 200-800 cm^{-1} as shown in **Fig. 4**. The Raman spectra show peaks appearing at 450 and 490 cm^{-1} corresponding to T_2g (2) and T_2g (3), respectively. It may be noted that both of these modes shift toward the higher wavenumber as the Zn is substituted with Ni in $Ni_{0.5}Zn_{0.5}FeCoO_4$ ferrite. The shift in the frequency of these modes strongly suggests that Ni substituted Zn ferrites possess inverse spinel structure. It may be mentioned that in Zn ferrite ($ZnFe_2O_4$) the Raman mode reported at 650 cm^{-1} (A_{1g}) is attributed to the symmetric stretch of Zn-O in ZnO_4 coordination, and the one around 660-700 cm^{-1} to FeO in FeO_4 coordination in magnetite (Fe_3O_4) [28, 29]. The Raman mode reported at 625 cm^{-1} (A_{1g}) is attributed to a symmetric stretch of $NiFe_2O_4$ for tetrahedral site, at 680 cm^{-1} (A_{1g}) for Fe_3O_4. In the present case, a broad peak corresponding to A_{1g} mode appears around 620-700 cm^{-1}.

Thermal characterization technique was used to get the optimum formation temperature for the sample. The thermogravimetric (TG) data and the corresponding scanning calirimetry analysis (DSC) curve are given from 30 to 900 °C in **Fig. 5**. The first exothermic process occurring near 205 °C is probably associated to the departure of water molecules during thermal decomposition of the precursor. In the range between 210 and 450°C, a major endothermic peak at ≈ 330°C in

DSC graph is due to the thermal effect for precursor decomposition and the maximum mass loss (Δm/m) occurred at this stage. So, this temperature (330 °C) is expected to be the crystallization temperature (T_c) of the material. The sample got free from all types of organic contaminants at ~680 C. The entire thermal effect was accompanied by the evolution of various gases (such as CO, CO2, water vapor, etc…), which was manifested by a single step weight loss, shown in the TG curves. Above 680º C, there was no significant thermal effect observed in the DSC curve and the corresponding TG curve showed no weight loss, implying the complete volatilization of carbon compounds.

3.3. Mössbauer measurement

The room temperature Mössbauer spectrum of $Ni_{0.5}Zn_{0.5}FeCoO_4$ ferrite is shown in **Fig. 6**. The solid lines represent the fit of a set of Lorentzian to the experimental data. The hyperfine parameters obtained from the fit to the spectrum including isomer shift (IS), quadrupole splitting (QS), full linewidth at half maximum (G), hyperfine magnetic field (H) and fractional area of each sub-spectrum (A) are given in **Table 1**. The spectrum was fitted with one sextet for the presence of Fe^{3+} in A-site, and two sextets for two octahedral B-sites, as it is usual in the case of Fe_2CoO_4 ferrites. The octahedral B1 and B2 sites have larger hyperfine magnetic field values than A-sites, as expected from literature for $CoFe_2O_4$ and $NiFe_2O_4$ ferrites[30, 31]. The hyperfine magnetic fields are very much reduced when compared to the above-mentioned ferrites, because our sample is doped with Zn that is diamagnetic. Small values of QS indicate that the sample was formed in adjacent cubic symmetry structure and did not distorted with the heat treatment. Superimposed to the sextets, two doublets are corresponding to two crystallographic sites of Fe^{3+} ions. One of the doublets, with hyperfine parameters of IS= 0.30 mm/s and QS=0.60 mm/s, is in accordance with literature for $NiFe_2O_4$ ferrite[32-33], which is not seen in the XRD pattern. The other doublet is super-paramagnetic indicating a small size of grains[30,31].

3.4. Electrical conductivity analysis

The frequency variation of the conductivity at different temperatures of $Ni_{0.5}Zn_{0.5}FeCoO_4$ ferrite is shown in **Fig. 7a**. This study can provide significant information about the conduction process of the sample. In the case of ferrite materials, the conduction process is generally due to the electron hopping between Fe^{2+} and Fe^{3+} ions present at the octahedral site. From **Fig. 7a**, we can observe a gradual increase of the conductivity with frequency. Indeed, the curves show a change in the conduction regime at a certain frequency, which is called hopping frequency $f_h \approx$

10^6 Hz. This hopping frequency moves towards high frequencies as the sintering temperature increases. For the frequencies $f < f_h$, the conductivity is independent of the frequency and it is in the form of a plateau. This frequency region corresponds to the *dc* conductivity (σ_{dc}), which is temperature dependent. The low conductive grain boundaries are more active in this frequency region; hence $Fe^{2+} \leftrightarrow Fe^{3+}$ electrons hopping are less. For $f > f_h$, the conductivity is frequency dependent and it increases exponentially. At this frequency region, the conductive grains become more active which promote the conduction mechanism. To verify these observations, we modeled the conductivity data using the following Jonscher's power-low[20, 21]:

$$\sigma(\omega) = \sigma_{dc} + A\omega^n \qquad (4)$$

where A and n are the pre-exponential and exponent factors, respectively. The modeling of experimental curves using Eq. (4) reveals a good agreement between the theoretical and the experimental curves of the studied sample (see **Fig. 7b**). The fitting results given in **Table 2** show an increase of the exponent n with temperature with values varying between 0.50±0.01and 0.604±0.01. This behavior is corresponding to a thermally activated process, and the conduction process in the sample follows the localized electrons hopping model.

3.5. Complex Impedance Spectroscopy (CIS)

Figure 8 show the real part of impedance (Z') variation with frequency and temperature for $Ni_{0.5}Zn_{0.5}FeCoO_4$ ferrite nanoparticle. The magnitude of Z' is typically higher in the low-frequency region and decreases gradually with increasing frequency. The value of Z' appears to merge in the high-frequency region independently of the temperature. We can interpret this result by the space charge when the charge barrier of the material has been reduced with the rise in temperature. This proves that the result of real impedance may be a responsible factor for the enhancement of conductivity of the material with temperature at high frequencies. The behavior of **Z'** observed for $Ni_{0.5}Zn_{0.5}FeCoO_4$ ferrite is in accordance with previously reported literature results for several spinel ferrites[21,35].

Fig. 9 shows the imaginary part of impedance variation (Z") with frequency at different temperatures. The curves show that Z" values reach a maximum ($Z"_{max}$) for all temperatures and we can note that the value of maximum imaginary of impedance $Z"_{max}$ shifts to higher frequencies with the increasing of temperature. A typical peak broadening which is slightly asymmetric in nature, can be observed with the rise in temperature. The broadening in the peaks confirms the temperature dependence of the electrical relaxation phenomena in the material[20, 21].

The activation energy conduction can be determined from the following Arrhenius relationship [35]:

$$f_{max} = f_0 \exp\left(-E_a / k_B T\right) \quad (5)$$

where f_0 is a pre-exponential factor, E_a the activation energy, k_B the Boltzmann constant and T is the temperature. The inset of **Fig. 9** illustrates the variation of f_{max} versus 1000/T. The activation energy value determined from the impedance spectrum is found to be 0.231±0.01 eV. Based on literature, the results of activation energies are in the same order of other spinel ferrite materials previously reported [21, 22].

To study the distribution of the relaxation, the normalized spectra of Z'' (i.e., Z''/Z''_{max}) as function of frequency at different temperatures are represented **(Fig.10)**. As one can see, the entire data of imaginary part of impedance can collapse into one master curve indicating that the relaxation dynamics does not change with temperature. This implies that the distribution of the relaxation has the same mechanism and the merging of all the curves indicates a possible release of space charge [20,36].

Fig. 11 depicts the Nyquist plots (i.e. Z'' vs. Z' plots) at different temperatures for $Ni_{0.5}Zn_{0.5}FeCoO_4$ ferrite. The analysis of such plots makes it possible to dissociate the contribution of grains and grain boundaries in transport phenomena in the sample. This separation is achieved by an adjustment of the Nyquist diagrams using an appropriate equivalent circuit. Generally, the complex ferrite systems do not always behave like ideal simple elements in impedance. For this reason, many electrical circuits have been introduced and interpreted in the literature [40, 41]. It is obvious in **Fig. 11** that for all the temperatures, the impedance spectra shows semicircle arcs whose maxima and diameters decline with the increase of temperature. The semicircles are the outcome of the conduction of the grain boundary, suggesting that the conduction process in our samples is principally related to the grain boundary contribution. To prove this observation, we modelized the complex impedance spectra. The suitable equivalent circuit configuration for the impedance plane plots is of the type of (R_g+R_{gb}//Z_{CPE}]) [41], as it is given in the inset of **Fig. 11**. In this arrangement, R_g and R_{gb} modelize the grain as well as the grain boundary resistances while Z_{CPE} modelizes the constant phase element impedance. The impedance response of a constant phase element (CPE) can be defined as[41]:

$$Z_{CPE} = \left[Q(j\omega)^{\alpha}\right]^{-1} \quad (6)$$

here, Q and α are the CPE parameters which are frequency independent. The R_g, R_{gb} Q and α parameters have been estimated for different temperatures by fitting the data using *Zview* software and they are presented in **Table 3**. It could be noted that the fit matches well with the experimental values (red solid lines in **Fig. 11**). From **Table 3**, one can see that the grain boundary resistance decreases with the increase of temperature, signalizing the semiconductor behavior of the sample. Furthermore, it has been proved that the values of R_{gb} are larger than R_g confirming that the conduction process in our sample is basically related to the grain boundary contribution as it is mentioned above.

3.6. Electrical modulus analysis

Fig. 12a shows the variation of the imaginary (M'') part of the dielectric modulus with frequency at different temperatures. In the available frequency range, the spectrum at each temperature exhibited one relaxation peak. The peaks shift systematically towards higher frequencies with an increase in temperature. The broadening of the peak indicates the spread of relaxation time with different (mean) time constants, and hence a non-Debye type of relaxation in the materials is observed, which is very much consistent with the impedance data [20]. To better understand the nature of the conduction mechanism and the effect of the bulk of grain boundary, the $M'' = f(M')$ curves are plotted in **Fig. 12b**. These curves reveal the presence of one semicircular arc for all temperatures. This behavior informs that the response is a result from grain interiors.

3.7. Dielectric studies

It is clear from **Fig. 13a and 13b** that the frequency dependence of imaginary part of permittivity ε'' (**Fig. 13a**) and loss factor *tan* δ (**Fig. 13b**) for $Ni_{0.5}Zn_{0.5}FeCoO_4$, have similar variations. For both samples, it is observed that ε'' and $tan\delta$ have high values at low frequencies while decrease with the increment in frequency and become independent at high frequencies. Similar results were observed for other ferrite systems [29, 30]. This type of dispersion in ε'' and *tan* δ plots is credited to the Maxwell-Wagner type of interfacial polarization in agreement with the Koop's phenomenological theory [31]. According to these theories, the dielectric structure of ferrite material is considered to be composing of two layers: grains and grain boundaries. Grains can be considered as areas having low electrical resistance due to perfect crystalline characteristics, while grain boundaries are the regions having high resistance. Maxwell Wagner interfacial polarization occurs in the grain boundaries due to the charge accumulation in these higher

resistive boundaries. This polarization occurs in all heterogeneous polycrystalline materials. At higher frequencies, this polarization diminishes and the value of dielectric constants becomes almost constant.

IV. Conclusion

The present work reports the results of structural characterization, Raman and Mössbauer, spectroscopy, electric and dielectric analyses of $Ni_{0.5}Zn_{0.5}FeCoO_4$ compound prepared by sol-gel method. XRD and Raman spectra confirm the crystalline nature and the formation of single-phase spinel ferrite. The inserted Zn amount can cause the cations redistribution between tetrahedral sites and octahedral sites and have a great effect on the structural and the electrical properties of as-prepared ferrite. Mössbauer spectroscopy revealed that hyperfine magnetic fields are very much reduced when compared to the above-mentioned ferrites, because our sample is doped with Zn that is diamagnetic. The electrical properties are found to be strongly dependent on temperature and confirmed the presence of one semicircular arc by the Nyquist plots. An electrical equivalent circuit formed by a parallel combination of grain resistance (R_b) and grain boundary resistances (R_{gb}) and constant phase element impedance (Z_{CPE}) was used to modelated this behavior. The analysis of the thermal variation of the imaginary part of the electrical modulus peak has indicated that the observed relaxation process is thermally activated. From these obtained results, we have deduced the evidence of a hopping mechanism in the conductivity behavior.

ACKNOWLEDGMENTS

This work is supported by:

- The Tunisian National Ministry of Higher Education, Scientific Research and Technology.
- The authors would like to acknowledge the financial support from FCT, Portugal (Project No. UID/CTM/50025/2013 I3N).
- This work was supported by funds from FEDER (Programa Operacional Factores de Competitividade COMPETE) and from FCT-Fundação para a Ciência e a Tecnologia

under the Project No. UID/FIS/04564/2016. Access to TAIL-UC facility (XRD, SEM and DSC) funded under QREN-Mais Centro Project No. ICT_2009_02_012_1890 is gratefully acknowledged.

References

[1] D. Stopples, J. Magn. Magn. Mater. 160(1) (1996) 323-328.

[2] E.C. Snelling, Soft Ferrites: Properties and applications, Butterworths, London, 1988.

[3] T. Hyeon, Chem. Commun. 8 (2003) 927-934.

[4] M. A. Willard, L. K. Kurihara, E. V. G. Harris, Int. Mater. Rev. 49 (2004) 125-170.

[5] Y. Wang, X. Wu,W. Zhang, W. Chen, J. Magn. Magn. Mater. 398 (2016) 90e95.

[6] C. Srinivas, B.V. Tirupanyam, D.L. Sastry, O.F. Caltun, J. Magn. Magn. Mater. 382 (2015) 15e19.

[7] R. Sahoo, S. Santra, C. Ray, S.K. Ray, T. Pal, New J. Chem. 40 (2016) 1861e1871.

[8] D. Moitra, B.K. Ghosh, S.R. Vadera, N.N. Ghosh, RSC Adv. 6 (2016) 14090e14096.

[9] P. Liu, Z. Yao, J. Zhou, RSC Adv. 5 (2015) 93739e93748.

[10] M.T. Rahman, M. Vargas, C.V. Ramana, J. Alloys Compd. 617 (2014) 547.

[11] G. Mustafa, M.U. Islam, M. Hussain, M. Ahmad, J. Alloys Compd. 618 (2015) 428-436.

[12] R.S. de Biasi, C. Larica, Solid State Commun. 144 (2007) 15–17.

[13] X. Wu, Z. Ding, N. Song, L. Li, W. Wang, Ceram. Int. 42 (2016) 4246–42455.

[14] P.N. Lisboa Filho, C.Vila, G.Petrucelli, W.A. Ortiz, E.Longo, Physica B 320 (2002) 249.

[15] W.D. Kingery, H.K. Bowen, D.R. Uhlman, Wiley, New York, 1976 (Chapter 18).

[16] K.R. Krishna, D. Ravinder, K.V. Kumar, A. Ch. Lincon, Matter Phys. 2153 (2012).

[17] J.L. Dormann, M. Nogues, J. Phys. Condens. Matter 2 (1990) 1223.

[18] N. Rezlescu, E. Rezlescu, C. Pasnicu, M.L. Craus, J. Phys. Condens. Matter 6 (1994) 5707.

[19] M. Pechini, US Patent 3, 330 (1967) 697.

[20] A. Omri, E. Dhahri, M. Es-Souni, M.A. Valente, L.C. Costa, J. Alloys Compd. 536 (2012) 173.

[21] S. Hcini, A.Omri, M. L.Bouazizi, A. Dhahri, K. Touileb. J.of Mat. Sci.: Mat. in Elect. 8674 (2018).

[22] A. Selmi, S. Hcini, H. Rahmouni, A. Omri, M.L. Bouazizi, A. Dhahri, Phase Transit. 90, 942 (2017)

[23] Y. Köseoğlu, F. Alan, M. Tan, R. Yilgin, M. Öztürk, Ceram. Int. 38 (2012) 3625.

[24] A. Iftikhar, M.U. Islam, M. Ahmad, S. Naseem, M.A. Iqbal, J. Alloy. Compd. 601 (2014) 116.

[25] A. Omri, M. Bejar, M. Sajieddine, E. Dhahri, E.K.Hlil, M. Es-Souni, Physica B 407 (2012) 2566.

[26] H. Lamsaf, A. Oulmekki, R. Fausto, B.F.O. Costa. J. of Phy. and Chemi. of Soli. (2018).

[27] H. Issaoui, A. Benali, M. Bejar, E. Dhahri, R. F. Santos, N. Kus., B. A. Nogueira. R. Fausto, B. F. O. Costa. J.of Super .and Nov. Magn. (2018) 4850.

[28] M. Popa, J. Franti, M. Kakihana. Solid State Ion. 154 (2002) 135.

[29] Y. Wang, J. Zhu, L. Zhang, X. Yang, X. Wang. Mater. Lett. 60 (2006) 1767.

[30] M.Al-Maasham et al, Hyp Inter. 15 (2018) 239.

[31] V.D. Sudheesh et al, Ceramics Inter (2017) 43.

[32] S.S.R. Inbanathan, V. Vaithyanathan, J. Arout Chelvane, G. Markandeyulu, K. Kamala Bharathi, J. Magn. Magn. Mater. 401 (2016) 370.

[33] S.S. Shinde, S.S. Meena, S.M. Yusuf, K.Y. Rajpure, J. Phys. Chem. C 115 (2011) 3731.

[34] K. Jalaiah, P.S.V. Subba Rao, B. Sreedhar. J. of Magn. and Magn. Materi. 91 (2017) 13.

[35] S. Hcini, A. Selmi, H. Rahmouni, A. Omri, M. L. Bouazizi. Cera. Intern. 16 (2016) 8.

[36] M.A. Valente, M. Peres, C. Nico, T. Monteiro, M.P.F. Graça, C.C. Silva. Opti. Mat. (2011).

[37] P. Córdoba-Torres, T.J. Mesquita, V. Roche, R.P. Nogueira. Electrochim Acta. 72 (2012) 172.

[38] B. Hirschorn, M.E. Orazema, B. Tribollet, I. Frateur, M. Musiani. Electrochim Acta. 55 (2010) 6218.

[39] P. B. Macedo, C. T. Moynihan, R. Bose, Phys. Chem.Glasses 13, (1972) 171.

[40] G. Williams and D. C. Watts, Trans. Faraday Soc. 66, (1970) 80.

[41] C.G. Koops, Phys. Rev. 83 (1951) 121.

[42] K. Funke, Prog. Solid State Chem. 22 (1993) 111–195.

[43] M.M. Costa, G.F.M. Pires Junior, A.S.B. Sombra, Mater. Chem. Phys., 123 (2010) 35.

Table and figure captions

Table 1: Mössbauer parameters resulting from the fit to the spectrum shown in Figure 7. The values in square parentheses were fixed during the fitting procedure.

Table 2: Fitting data of the conductivity of $Ni_{0.5}Zn_{0.5}FeCoO_4$ ferrite.

Table 3: Electrical parameters of equivalent circuit deduced from complex impedance spectra for different temperatures for $Ni_{0.5}Zn_{0.5}FeCoO_4$ ferrite.

Figure 1: XRD pattern of $Ni_{0.5}Zn_{0.5}FeCoO_4$ ferrite. All peaks are indexed in the cubic spinel type structure with Fd-3m space group.

Figure 2: (a) SEM Micrographs and (b) Gaussian distribution of particle sizes of $Ni_{0.5}Zn_{0.5}FeCoO_4$ ferrite.

Figure 3: The EDAX analysis spectrum at room temperature of $Ni_{0.5}Zn_{0.5}FeCoO_4$ compound.

Figure 4: Room temperature Raman spectra of $Ni_{0.5}Zn_{0.5}FeCoO_4$ ferrite.

Figure 5: Thermogravimetric analysis (TGA, blue line) and Differential Scanning Calorimetry (DSC, black line) curves of the $Ni_{0.5}Zn_{0.5}FeCoO_4$ ferrite.

Figure 6: Room temperature Mössbauer spectrum of $Ni_{0.5}Zn_{0.5}FeCoO_4$ ferrite and fitted curves describing the experimental data.

Figure 7: **(*a*)** Variation of the total conductivity as a function of frequency at different temperatures for $Ni_{0.5}Zn_{0.5}FeCoO_4$ ferrite. **(*b*)** Variation of the total conductivity versus frequency at T = 150 K. Red solid lines represent the fitting to the experimental data using the universal Jonscher power law. The inset shows the variation of exponent *n* with respect to all temperatures.

Figure 8: Variation of real part of the impedance (Z') of the $Ni_{0.5}Zn_{0.5}FeCoO_4$ ferrite as a function of frequency for different temperatures.

Figure 9: Variation of imaginary part of the impedance (Z'') of $Ni_{0.5}Zn_{0.5}FeCoO_4$ ferrite as a function of frequency for different temperatures. The inset shows the Arrhenius plots f_{max} vs.1000/T.

Figure 10: Scaling behavior of Z" at various temperatures for $Ni_{0.5}Zn_{0.5}FeCoO_4$ ferrite.

Figure 11: Complex impedance spectra for $Ni_{0.5}Zn_{0.5}FeCoO_4$ ferrite at several temperatures with electrical equivalent circuit (see the inset).

Figure 12: **(a)** Variation of M'' with frequency at different temperatures for the $Ni_{0.5}Zn_{0.5}FeCoO_4$ ferrite. **(b)** Cole–Cole plots between M' and M'' measured at various temperatures.

Figure 13: **(a)** Variation of the imaginary part of dielectric constant versus frequency for the $Ni_{0.5}Zn_{0.5}FeCoO_4$ ferrite. **(b)** Variation of loss tangent (*tanδ*) with angular frequency at different temperatures of $Ni_{0.5}Zn_{0.5}FeCoO_4$ ferrite.

Conflict of Interest and Authorship Conformation Form

Please check the following as appropriate:

- All authors have participated in (a) conception and design, or analysis and interpretation of the data; (b) drafting the article or revising it critically for important intellectual content; and (c) approval of the final version.

- This manuscript has not been submitted to, nor is under review at, another journal or other publishing venue.

- The authors have no affiliation with any organization with a direct or indirect financial interest in the subject matter discussed in the manuscript

- The following authors have affiliations with organizations with direct or indirect financial interest in the subject matter discussed in the manuscript:

Author's name	Affiliation
Aref Omri	Faculty of Science and Technology of Sidi Bouzid, Tunisia
Essebti Dhahri	Faculty of sfax, Tunisia
Benilde Costa	Physics Department, University of Coimbra, Portugal
Manuel de Almeida Valente	Physics Department, University of Aveiro, Portugal

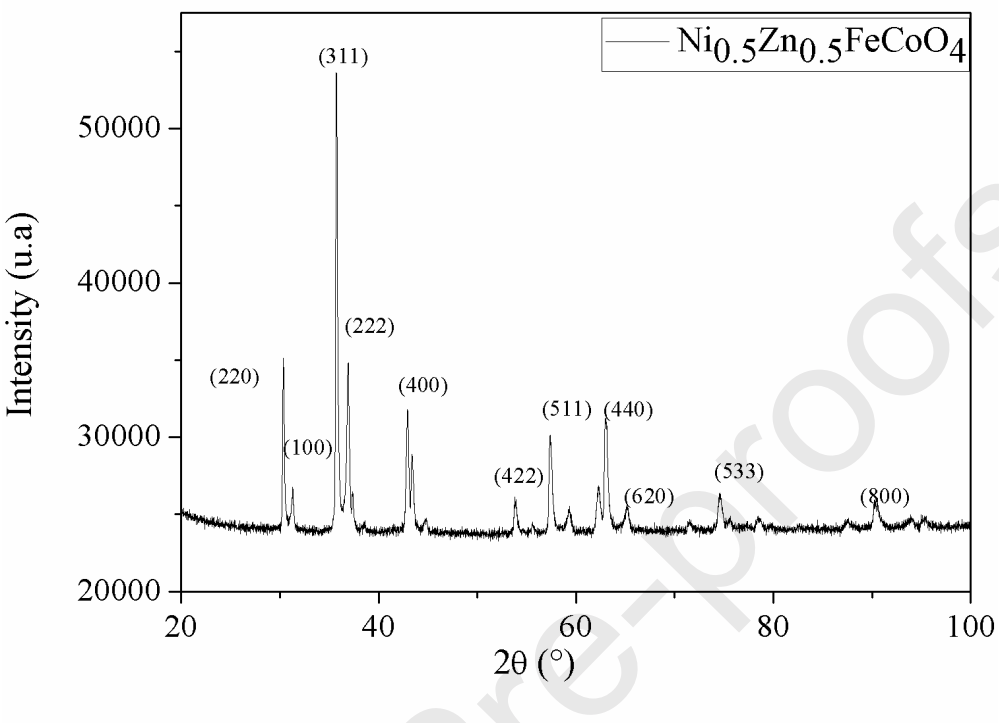

Fig. 1

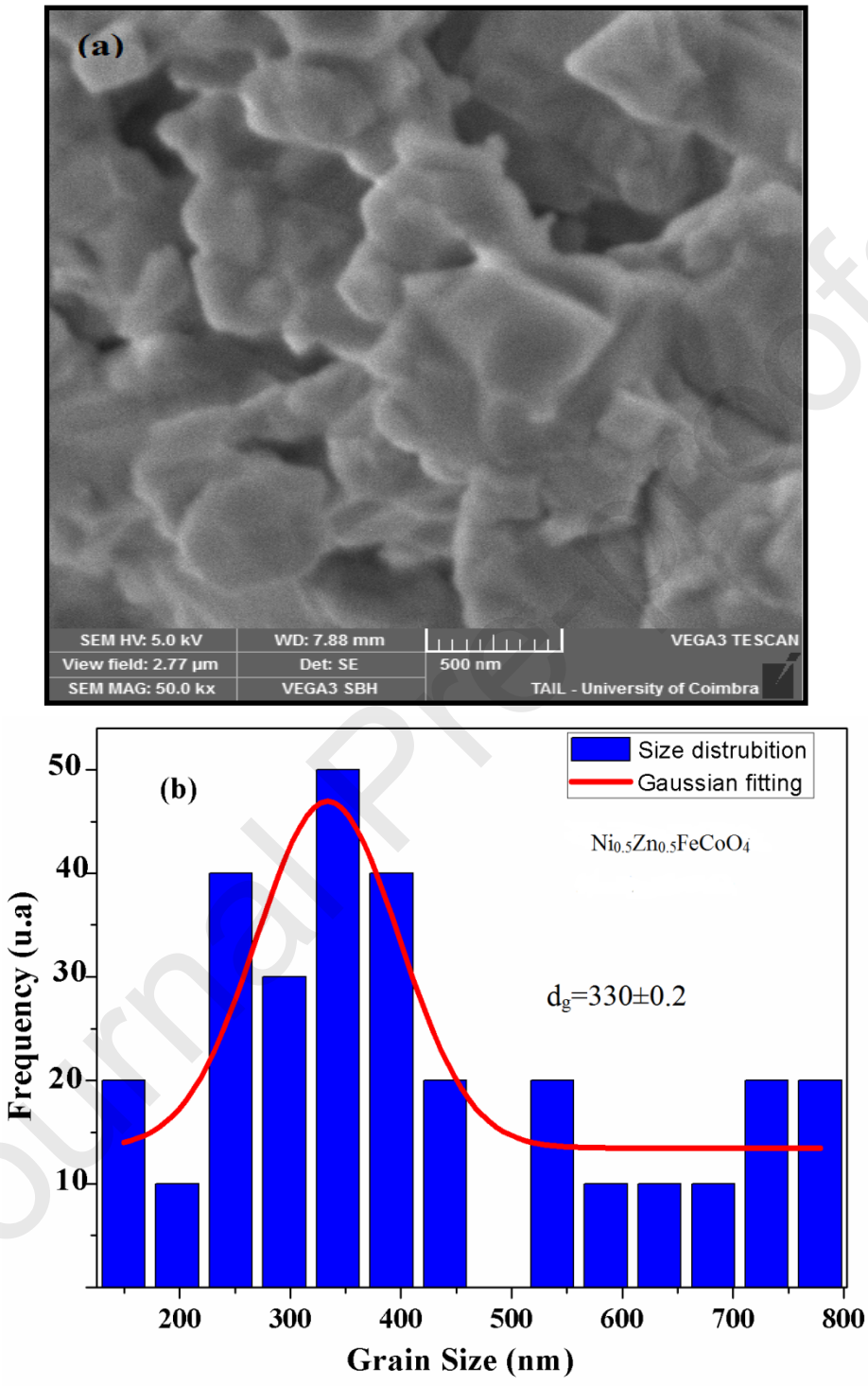
(a)
SEM HV: 5.0 kV
WD: 7.88 mm
VEGA3 TESCAN
View field: 2.77 µm
Det: SE
500 nm
SEM MAG: 50.0 kx
VEGA3 SBH
TAIL - University of Coimbra
(b)
Size distrubition
Gaussian fitting
Ni0.5Zn0.5FeCoO4
dg=330±0.2
Frequency (u.a)
Grain Size (nm)
10
20
30
40
50
200
300
400
500
600
700
800

Fig. 2

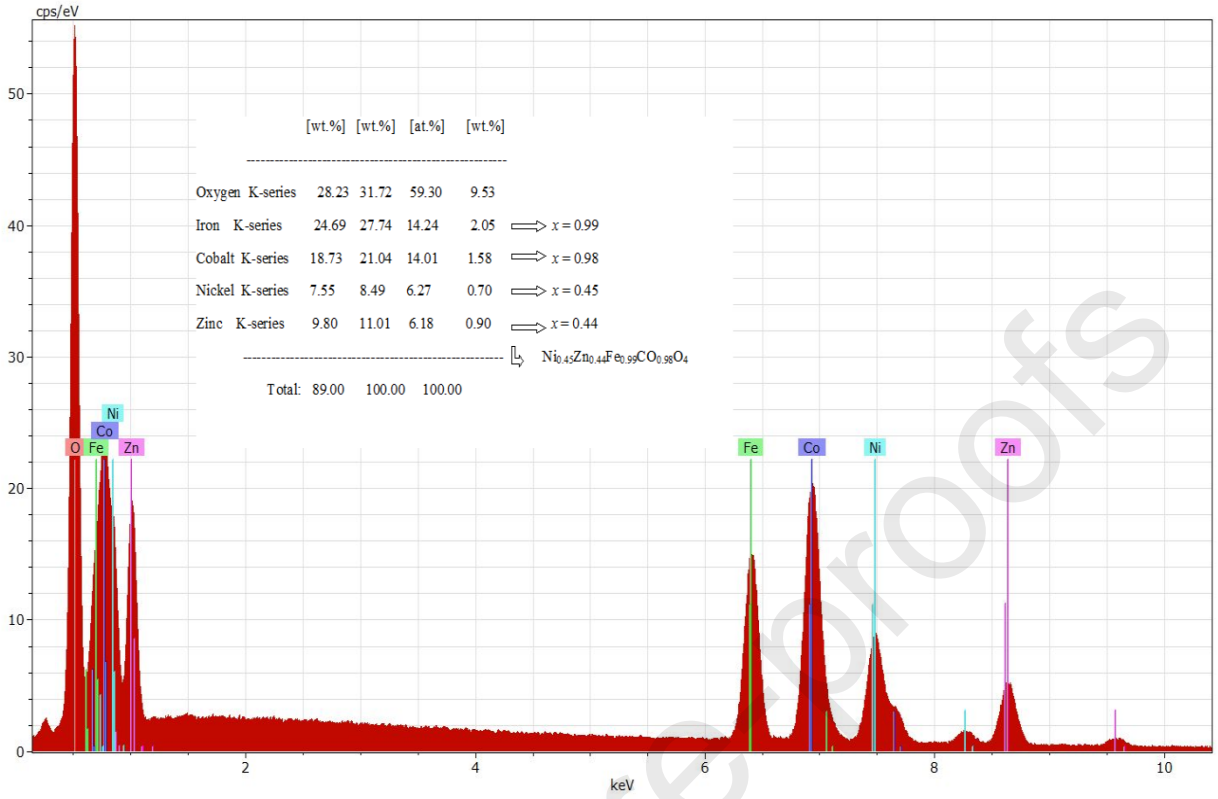

Fig. 3

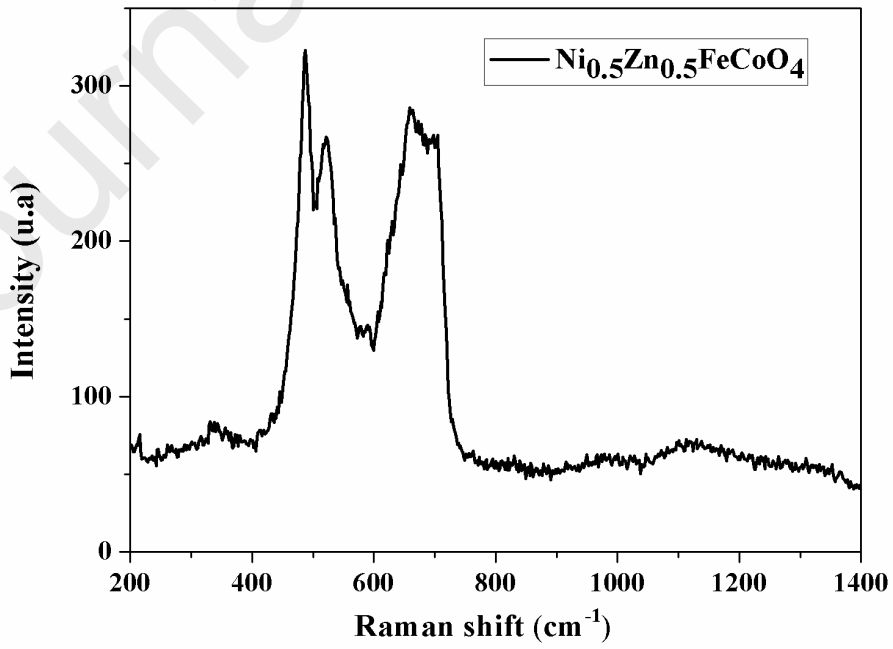

Fig. 4

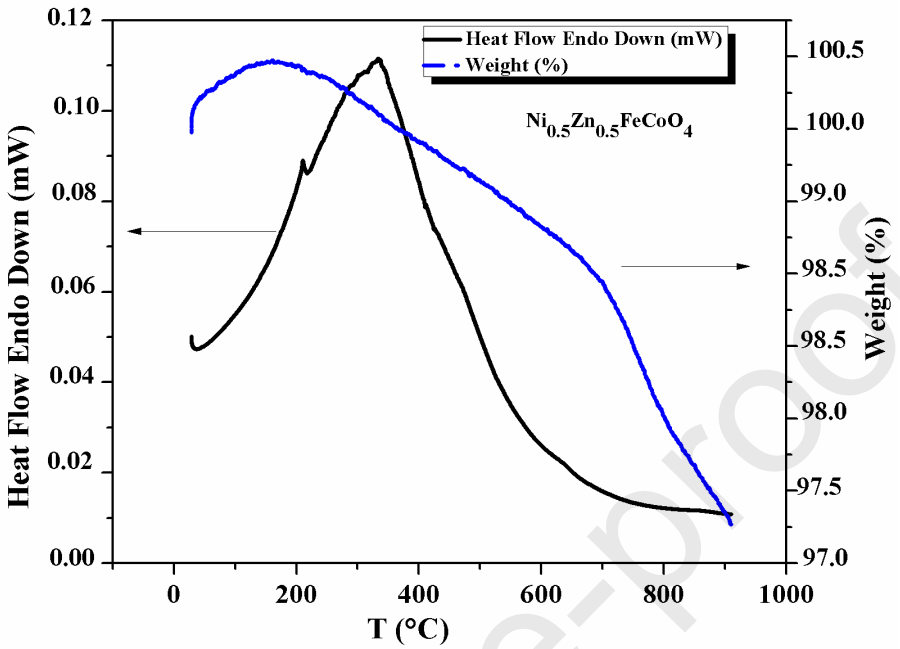

Fig. 5

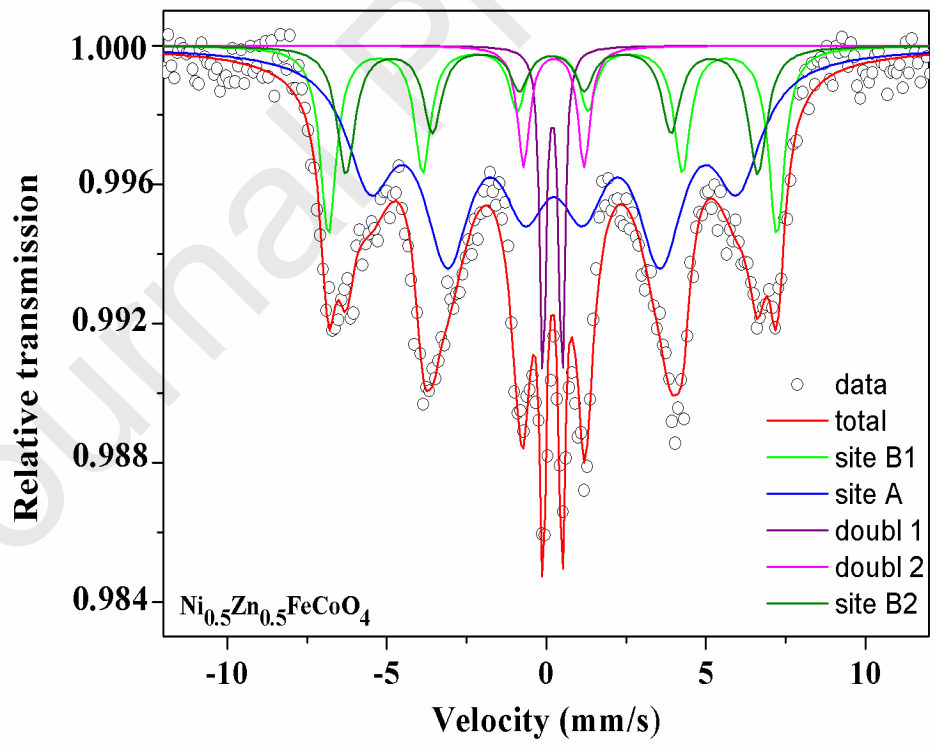

Fig. 6

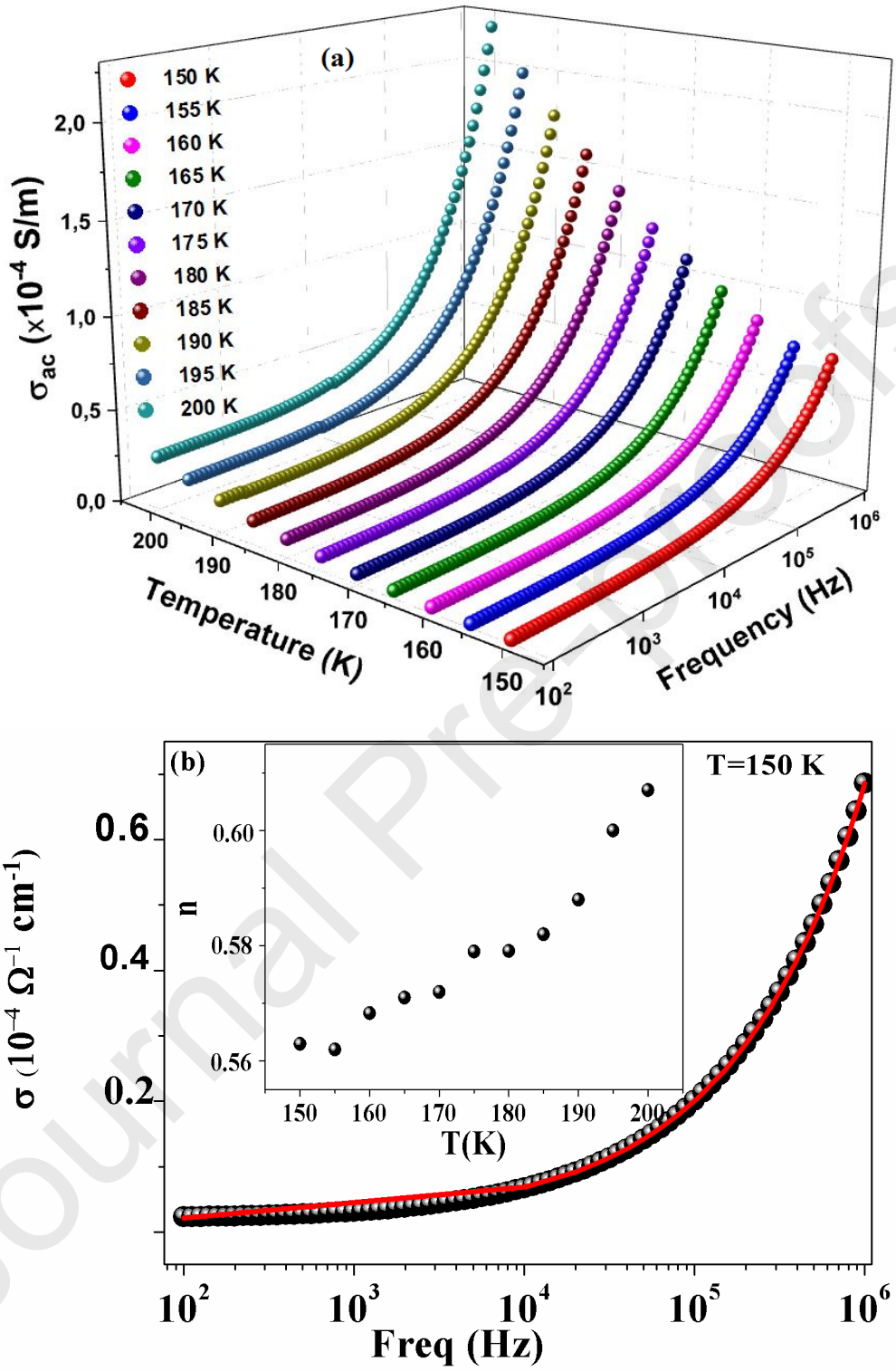
(a)
150 K
155 K
160 K
165 K
170 K
175 K
180 K
185 K
190 K
195 K
200 K
σac (x10-4 S/m)
2,0
1,5
1,0
0,5
0,0
200
190
180
170
160
150
Temperature (K)
10²
10³
10⁴
10⁵
10⁶
Frequency (Hz)
(b)
T=150 K
σ (10-4 Ω-1 cm-1)
0.6
0.4
0.2
n
0.60
0.58
0.56
150
160
170
180
190
200
T(K)
10²
10³
10⁴
10⁵
10⁶
Freq (Hz)

Fig. 7

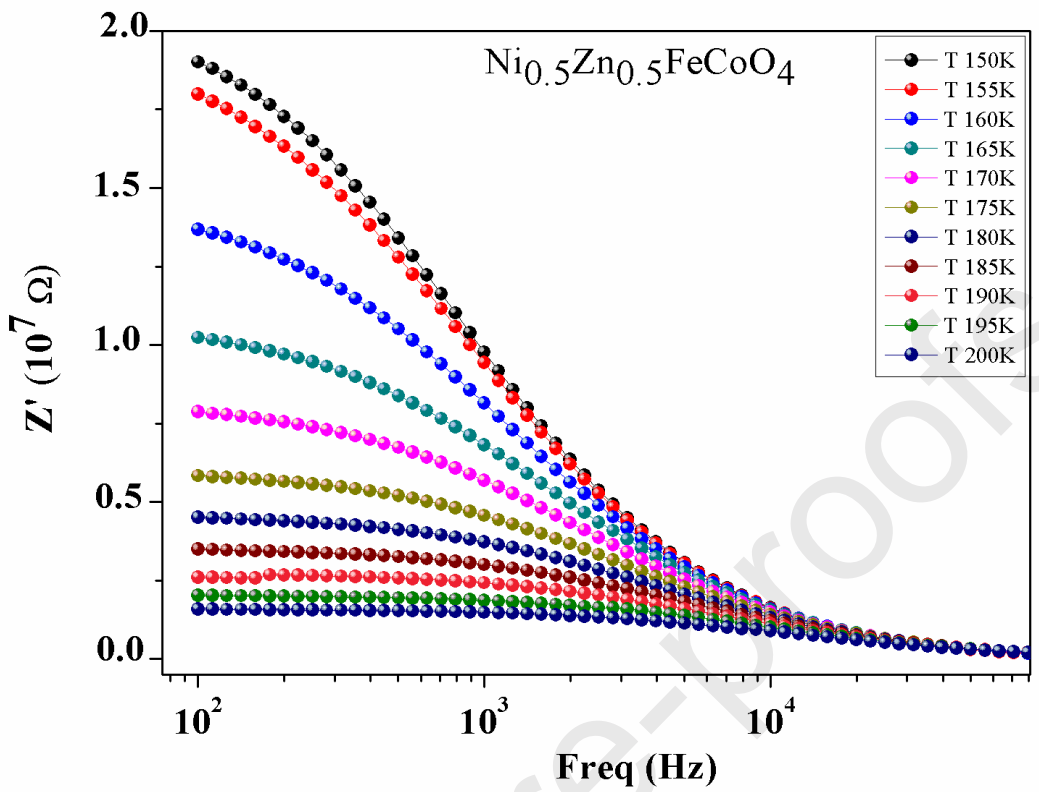
Ni0.5Zn0.5FeCoO4
T 150K
T 155K
T 160K
T 165K
T 170K
T 175K
T 180K
T 185K
T 190K
T 195K
T 200K
Z' (10^7 Ω)
Freq (Hz)

Fig. 8

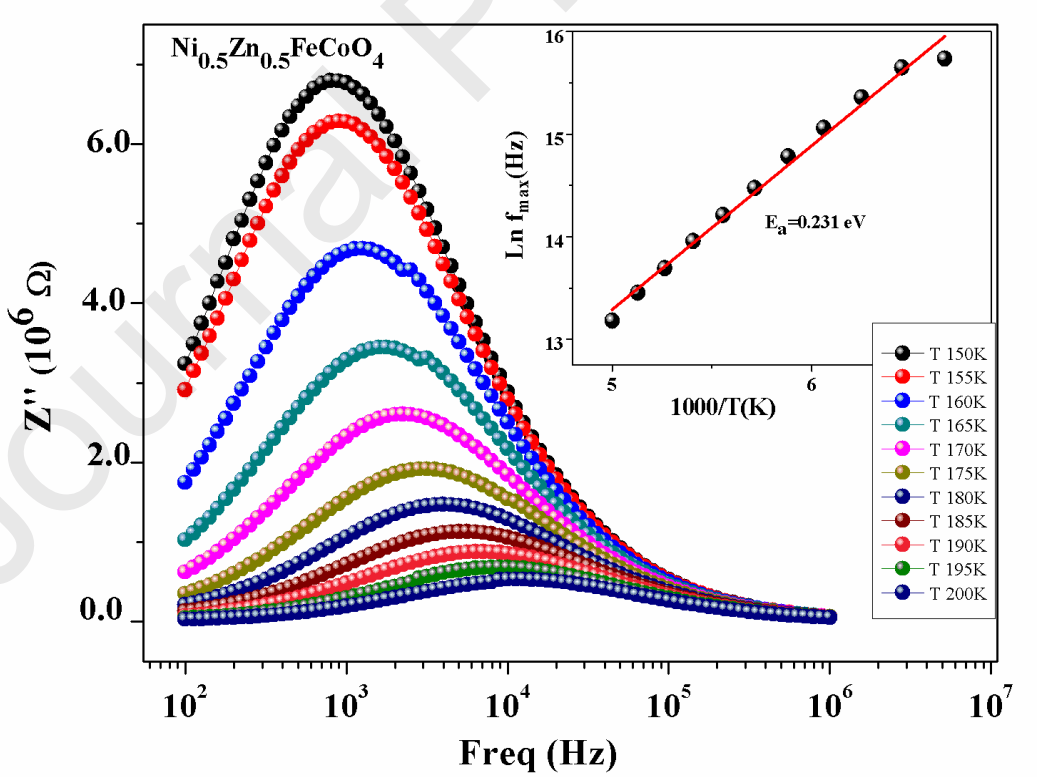
Ni0.5Zn0.5FeCoO4
Z'' (10^6 Ω)
Freq (Hz)
Ln f_max(Hz)
1000/T(K)
Ea=0.231 eV
T 150K
T 155K
T 160K
T 165K
T 170K
T 175K
T 180K
T 185K
T 190K
T 195K
T 200K

Fig. 9

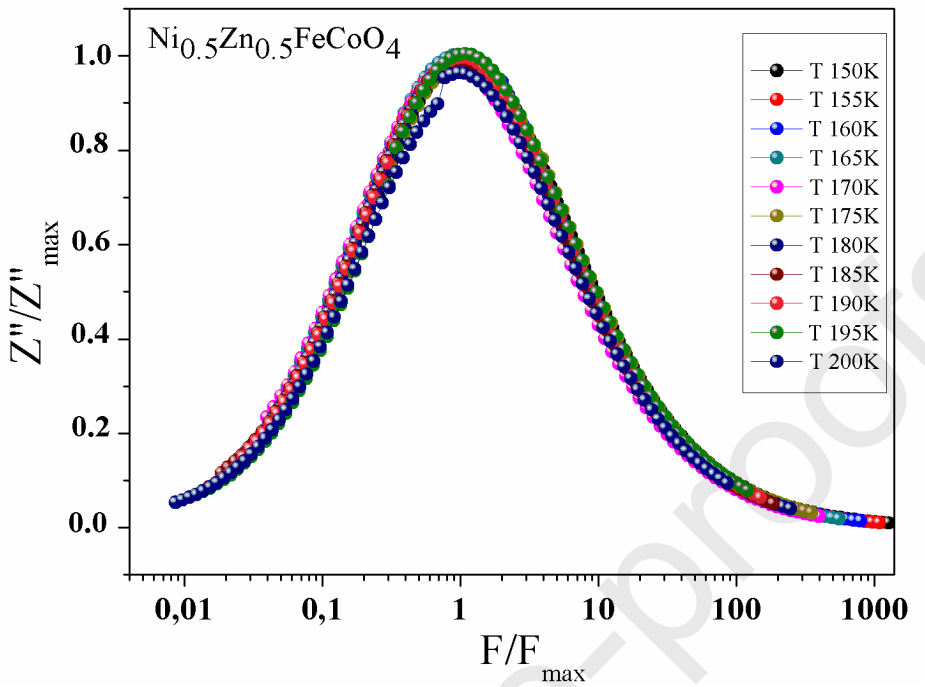

Fig. 10

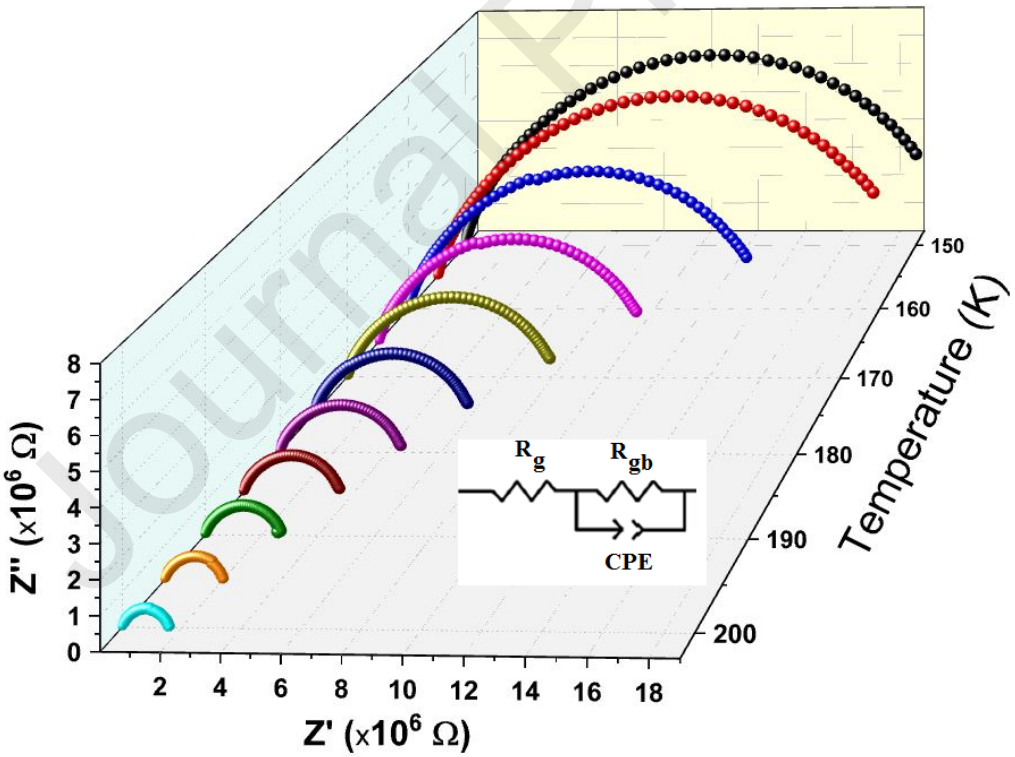

Fig. 11

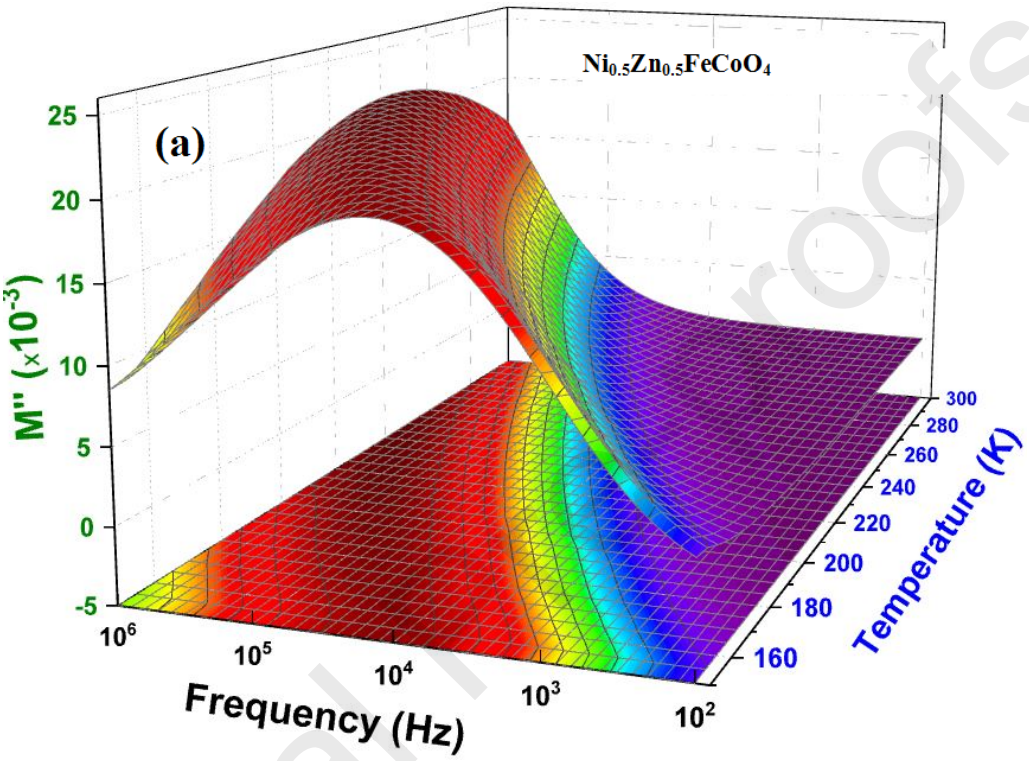

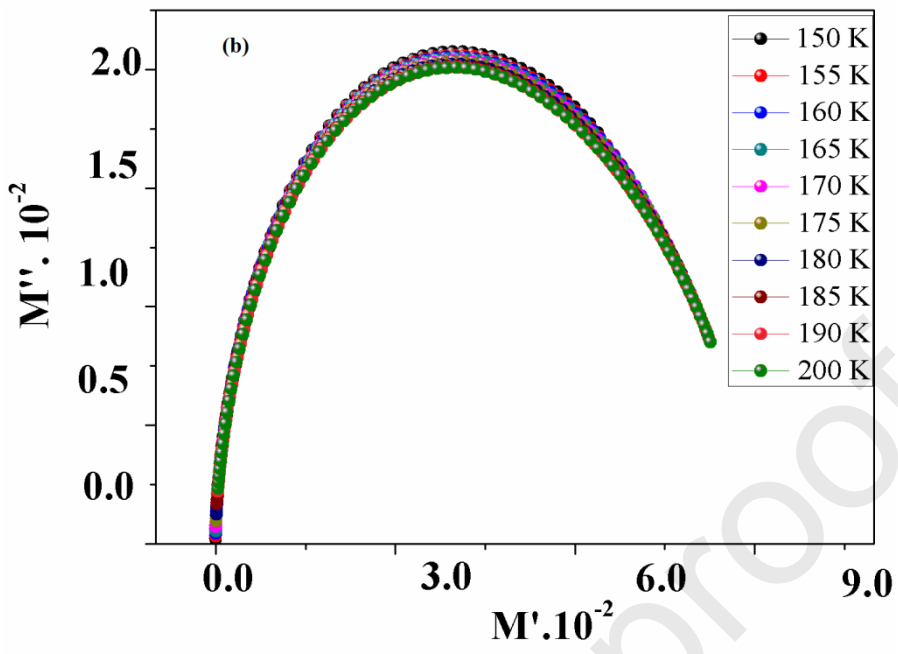

Fig. 12

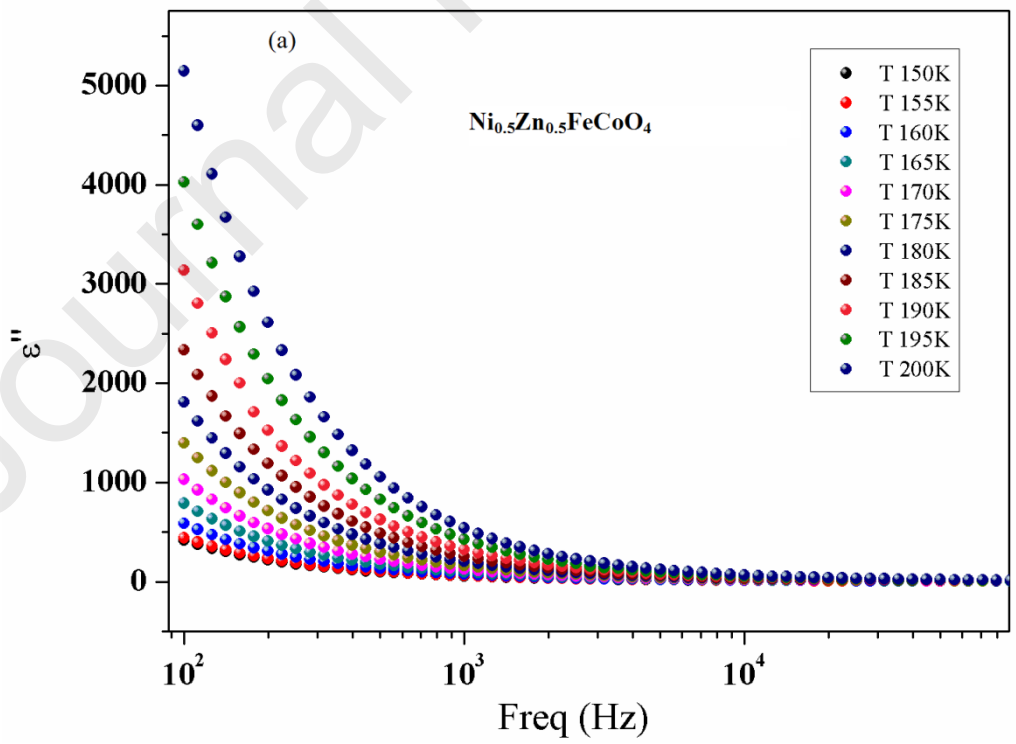

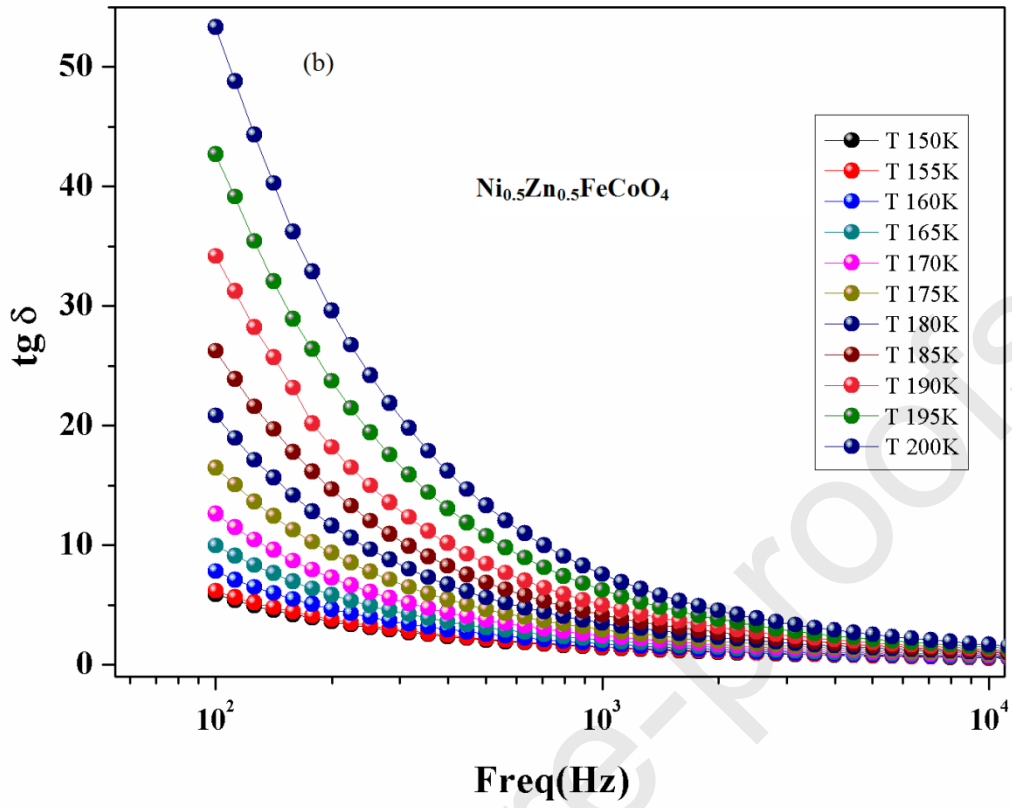

Fig. 13

Table 1

IS (mm/s)	QS (mm/s)	H(T)	G (mm/s)	A (%)	Site
0.35(1)	[0.00]	35.7(1)	1.71(1)	59.1	Site A (Tetra)- Sextet 1
0.30(1)	-0.001(1)	43.5(1)	0.61(1)	17.5	Site B1 (Octa)- Sextet 2
0.29(1)	-0.008(1)	[40.0]	0.47(1)	13.5	Site B2 (Octa)- Sextet 3
0.30(1)	0.60(1)	-	0.22(1)	5.6	Fe^{3+} (Ni_2CoO_4)- Doublet 1
0.34(1)	1.90(1)	-	0.68(1)	4.3	Fe^{3+} - Doublet 2

Nomenclature: IS-isomer shift; QS- quadrupole splitting, H- hyperfine magnetic field, G- fullwidth at half maximum of Lorentzians, A- area under subspectrum

Table 2

T (K)	150	155	160	165	170	175	180	185	190	195	200
σ_{dc} (10^{-8} S.m^{-1})	2.794	2.897	3.030	3.298	3.732	3,764	4.313	4.567	4.683	4.420	4,407
A (x 10^{-6})	1.801	1.973	2.667	3.697	4.933	6.887	8.974	11.779	15.453	20.746	27.032
n	0.563	0.562	0.5683	0.571	0.572	0.579	0.5791	0.582	0.588	0.600	0,607

Table 3

T (K)	150	155	160	165	170	175	180	185	190	195	200
R_g (Ω)	360.2	315.58	282.44	235.25	183.45	125.6	87.67	53.51	27.44	8.58	2.69
R_{gb} *10^7(Ω)	1.911	1.526	1,357	0.954	0.778	0.579	0.449	0.348	0.270	0.205	0.160
CPE*10^{-11}(F)	4.058	4.284	4.766	5.441	6.601	7.469	8.755	9.964	10.991	11.601	13.162
α	0.804_1	0.800_7	0.795	0.783	0.777	0.772	0.764	0.759	0.754	0.753	0.748

- The $Ni_{0.5}Zn_{0.5}FeCoO_4$ spinel ferrite is synthesized by a sol-gel technique.
- The temperature and frequency dependence of dielectric constants have been investigated.
- The electrical properties are found to be strongly dependent on temperature and confirmed the presence of one semicircular arc by the Nyquist plots.

- The analysis of the thermal variation of the imaginary part of the electrical modulus peak has indicated that the observed relaxation process is thermally activated.